

NeuroMamba: Multi-Perspective Feature Interaction with Visual Mamba for Neuron Segmentation

Liuyun Jiang, Yizhuo Lu, Yanchao Zhang, Jiazheng Liu, and Hua Han

Abstract— Neuron segmentation is the cornerstone of reconstructing comprehensive neuronal connectomes, which is essential for deciphering the functional organization of the brain. The irregular morphology and densely intertwined structures of neurons make this task particularly challenging. Prevailing CNN-based methods often fail to resolve ambiguous boundaries due to the lack of long-range context, whereas Transformer-based methods suffer from boundary imprecision caused by the loss of voxel-level details during patch partitioning. To address these limitations, we propose NeuroMamba, a multi-perspective framework that exploits the linear complexity of Mamba to enable patch-free global modeling and synergizes this with complementary local feature modeling, thereby efficiently capturing long-range dependencies while meticulously preserving fine-grained voxel details. Specifically, we design a channel-gated Boundary Discriminative Feature Extractor (BDFE) to enhance local morphological cues. Complementing this, we introduce the Spatial Continuous Feature Extractor (SCFE), which integrates a resolution-aware scanning mechanism into the Visual Mamba architecture to adaptively model global dependencies across varying data resolutions. Finally, a cross-modulation mechanism synergistically fuses these multi-perspective features. Our method demonstrates state-of-the-art performance across four public EM datasets, validating its exceptional adaptability to both anisotropic and isotropic resolutions. The source code will be made publicly available.

Index Terms— Anisotropy, deep learning, electron microscopy, mamba, neuron segmentation.

I. INTRODUCTION

NEURON segmentation serves as the cornerstone of connectomics, enabling the reconstruction of synapse-level neural circuits to decipher the functional organization of the brain [1] and advance our understanding of biological neural functions [2]–[4]. Currently, volumetric electron microscopy

This work was supported by the grants from the STI 2030-Major Projects (2021ZD0204500, 2021ZD0204503), the National Natural Science Foundation of China (32171461).

Liuyun Jiang, Yizhuo Lu, Yanchao Zhang and Hua Han are with State Key Laboratory of Brain Cognition and Brain-Inspired Intelligence Technology, Institute of Automation, Chinese Academy of Sciences, Beijing, China, and also with School of Future Technology, University of Chinese Academy of Sciences, Beijing, China (e-mail: jiangliuyun2023@ia.ac.cn; luyizhuo2023@ia.ac.cn; zhangyanchoa2021@ia.ac.cn; hua.han@ia.ac.cn).

Jiazheng Liu is with State Key Laboratory of Brain Cognition and Brain-inspired Intelligence Technology, Institute of Automation, Chinese Academy of Sciences, Beijing, China (e-mail: liujiazheng2018@ia.ac.cn).

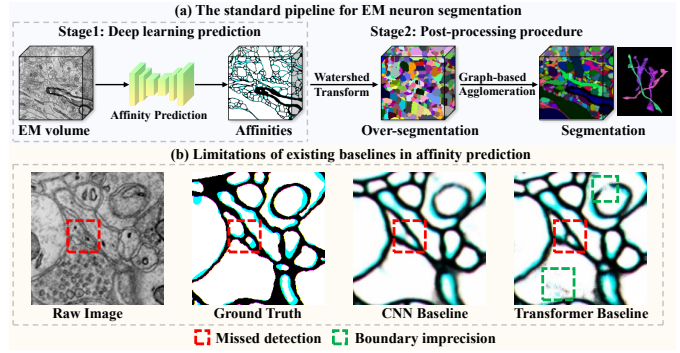


Fig. 1: Illustration of the standard EM neuron segmentation pipeline and limitations of existing baselines. (a) The standard two-stage pipeline: deep learning-based affinity prediction followed by post-processing. (b) Complementary failures in affinity prediction. The CNN baseline misses ambiguous membranes due to limited context (red box), while the Transformer baseline suffers from boundary imprecision due to the loss of voxel details caused by patch partitioning (green boxes).

(EM) at nanometer resolution remains the premier technique capable of capturing the intricate morphology of neurons and individual synapses within brain tissue [5], [6]. However, even small volumes of neural tissue produce vast amounts of data at this resolution [7]–[9], rendering manual reconstruction prohibitively time-consuming and labor-intensive, creating an urgent demand for efficient automated segmentation methods.

To overcome these obstacles, automated methods based on deep learning have been extensively developed [10]–[13]. Currently, the prevailing paradigm follows a two-stage boundary detection framework, as illustrated in Fig. 1(a). In this pipeline, a deep neural network first predicts voxel-wise affinities [14], which are subsequently processed by post-processing algorithms [11], [15], [16] to generate the final instance segmentation. Despite these advancements, achieving accurate reconstruction remains a significant hurdle. The complex morphology, dense branching, and diverse textures of neurons demand a model that can capture both fine-grained local details for precise boundary detection and long-range spatial dependencies for structural continuity. This dual requirement exposes the fundamental limitations of prevailing deep learning architectures, as highlighted in Fig. 1(b). On the one hand, Convolutional Neural Networks (CNNs) [10], [11],

while effective at extracting local features, are constrained by their inherent locality. Their limited receptive fields often fail to capture sufficient context to resolve ambiguous boundaries (as seen in the red box), making them prone to topological errors such as erroneous splits. On the other hand, Transformer-based methods [17]–[20] leverage global context via the attention mechanism to better resolve ambiguous regions. However, this patch-based paradigm often neglects crucial correlations among voxels within each patch, leading to boundary imprecision (as seen in the green box). Furthermore, standard Transformers often struggle to adapt to the anisotropic resolution of 3D EM data, where significant discrepancies between transverse and axial resolutions complicate voxel affinity modeling. Consequently, a clear and urgent need exists for a novel architecture capable of efficiently and holistically modeling both global continuity and local details without the inherent drawbacks of existing approaches.

The Mamba architecture [21], built upon state space models (SSMs) [22], has recently emerged as a compelling successor to Transformers for efficient long-sequence modeling. Mamba distinguishes itself by its ability to capture long-range dependencies with linear complexity. This unique attribute offers a paradigm-shifting advantage for neuron segmentation: it enables the modeling of global voxel dependencies across entire volumetric blocks without the need for patch partitioning. By processing the raw volume directly, Mamba inherently preserves the intrinsic voxel-level spatial continuity that Transformers often sacrifice. However, while Mamba provides an ideal backbone, its standard scanning mechanisms treat all spatial dimensions uniformly. This generic approach fails to explicitly account for the pronounced anisotropy typical of EM data, where the axial resolution is often much lower than that of the transverse plane. Consequently, the distinct spatial relationships in neuronal structures cannot be optimally modeled by existing scanning strategies, highlighting the critical need for a mechanism tailored to differentiate and dynamically balance transverse and axial features.

In this paper, we propose NeuroMamba, a novel framework designed for accurate neuron segmentation by synergistically integrating local morphological cues with global spatial contexts. Specifically, we first design a channel-gated Boundary Discriminative Feature Extractor (BDFE) to capture fine-grained local details. This module enhances boundary precision across multiple channels, ensuring that delicate neuronal membranes are not overlooked. Complementing this local feature modeling, we introduce the Spatial Continuous Feature Extractor (SCFE) to efficiently model long-range voxel dependencies. Within this module, we incorporate a resolution-aware scanning mechanism into the Visual Mamba architecture to specifically address the limitations of generic scanning strategies in handling anisotropy. By utilizing resolution priors, this mechanism dynamically balances the modeling of transverse and axial features, enabling adaptive global modeling without patch partitioning. Finally, these multi-perspective features are synergistically integrated via a Cross Feature Interaction (CFI) module using a cross-modulation mechanism, yielding robust and accurate affinity predictions.

The main contributions of this paper are summarized as

follows:

- We propose NeuroMamba, a novel multi-perspective framework that synergizes the linear complexity of Mamba for patch-free global modeling with complementary local feature modeling. This architecture effectively overcomes the receptive field limitations of CNNs and the boundary imprecision issues of patch-based Transformers.
- We design two specialized feature extractors and a feature interaction module: the BDFE enhances fine-grained morphological details, the SCFE models long-range voxel dependencies, and the CFI dynamically fuses these complementary features via cross-modulation.
- We introduce a novel resolution-aware scanning mechanism to address the inflexibility of generic scanning strategies. By incorporating resolution priors, this mechanism dynamically balances the modeling of transverse and axial features to adaptively model spatial dependencies across varying data resolutions, ranging from isotropic to highly anisotropic.
- Our method achieves state-of-the-art performance on four public EM datasets, demonstrating exceptional adaptability to both anisotropic and isotropic resolutions.

II. RELATED WORK

A. Neuron Segmentation

Deep learning-based approaches for neuron segmentation are broadly categorized into object-tracking-based and boundary-detection-based methods. Object-tracking-based methods [12], [23], [24] reconstruct neurons individually, a process that is often computationally intensive. In contrast, boundary-detection-based methods have become the predominant paradigm; they first predict voxel affinities and then apply post-processing techniques [15], [16] to segment neurons, offering a more computationally efficient alternative.

Within this paradigm, CNNs have served as the foundational architecture [10], [11], [25]–[27]. Despite significant advances, these models are inherently constrained by their local receptive fields, which limits their ability to capture the long-range dependencies required to maintain the continuity of tortuous neuronal processes.

To address this core limitation of locality, architectural paradigms that integrate Vision Transformers with U-shaped networks, exemplified by models such as UNETR [19] and SwinUNETR [20], have been introduced to the field [17], [18]. By modeling global dependencies between image patches, they can better preserve structural continuity. However, this patch-based approach presents inherent limitations. It often neglects fine-grained, voxel-level correlations within each patch, thereby compromising boundary precision. Furthermore, these models typically require extensive pre-training on large-scale datasets and exhibit limited adaptability to the anisotropic characteristics of EM data [17]. These complementary weaknesses of CNNs and Transformers highlight a clear need for a new architecture that can efficiently and holistically model both local details and global context.

B. Visual Mamba

Mamba [21], built upon state space models (SSMs) [22], has recently emerged as a compelling successor to Transformers for long-sequence modeling. It achieves linear complexity while demonstrating exceptional capability in capturing long-range dependencies, which has facilitated its rapid adoption in computer vision [28]–[31] and medical image segmentation. Initial works like U-Mamba [32] and SegMamba [33] successfully integrated Mamba blocks into U-Net architectures, demonstrating promising results on various 2D and 3D medical imaging tasks.

The application of Mamba has also been explored in the challenging domain of EM image segmentation. ViM-UNet [34] was the first to adapt Mamba for 2D EM segmentation, while EMmamba [35] adopted the TSMamba block from SegMamba, leveraging pre-training to tackle the task of 3D EM segmentation. However, a critical limitation of these pioneering methods is their reliance on generic scanning mechanisms. As a core component, the scanning mechanism not only enhances computational efficiency but also encodes vital task-specific spatial information. Existing approaches either adopt scanning strategies from 2D applications (e.g., bidirectional scan [28]), video processing (3D bidirectional scan [36]), or other domains like object detection (e.g., Hilbert scan [37], [38]).

These generalized scanning strategies are suboptimal for 3D neuron segmentation because they do not explicitly account for the pronounced anisotropy present in most EM volumes. The complex, intertwining morphology of neurons requires a more nuanced approach to modeling spatial relationships. Consequently, the development of scanning mechanisms specifically tailored to differentiate and dynamically balance the modeling of transverse and axial features in EM data remains a critical and unexplored research direction.

III. METHOD

In this section, we present the technical details of NeuRoMamba. We first formally define the neuron segmentation task. Then, we introduce the three core components of our proposed Multi-Perspective Feature Interaction (MPFI) block, as illustrated in Fig. 3: (1) the Boundary Discriminative Feature Extractor (BDFE), designed to capture fine-grained local boundary cues; (2) the Spatial Continuous Feature Extractor (SCFE), engineered to model long-range global dependencies without patching; and (3) the Cross Feature Interaction (CFI) module, which synergistically fuses these complementary features.

A. Problem Definition

Given a 3D EM image volume $\mathbf{I} \in \mathbb{R}^{D \times H \times W}$, the task of neuron segmentation is to predict the identity of each voxel, denoted as $\mathbf{S} \in \mathbb{N}^{D \times H \times W}$, where D , H , and W represent the depth, height, and width of the volume, respectively. Each voxel's ID in \mathbf{S} indicates the specific neuron to which it belongs, with ID 0 representing the background. We follow a two-stage boundary detection approach to predict the affinity $\mathbf{A} \in [0, 1]^{3 \times D \times H \times W}$, which represents the probability that

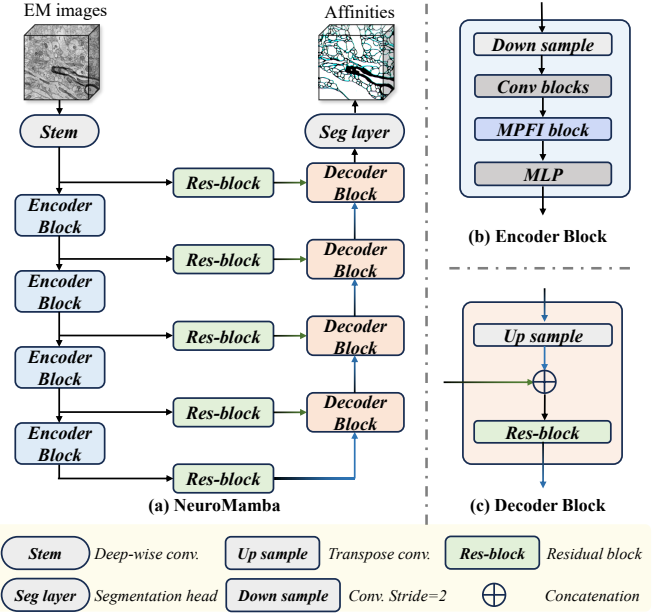


Fig. 2: Architecture of the proposed NeuroMamba. (a) The overall pipeline of NeuroMamba. (b) Details of the Encoder Block, where we introduce the MPFI block for multi-perspective modeling. (c) Details of the Decoder Block.

adjacent voxels in the three directions belong to the same neuron. Subsequently, a post-processing step is applied to the affinity \mathbf{A} to obtain the final neuron instance segmentation result \mathbf{S} .

B. BDFE:Boundary Discriminative Feature Extractor

To improve the accuracy of neuron boundary segmentation, especially in densely packed regions, we introduce a channel-gated module designed to enhance the extraction of neuronal morphological features. This module improves the model's ability to capture voxel affinities in fine-grained structures, thereby reducing merge and split errors in the final segmentation. A key challenge in this task stems from the elongated morphology of neurons. For such long-range, anisotropic structures, the large, square pooling windows employed in conventional CNNs [10], [11] often incorporate extraneous information from adjacent yet unrelated regions, which can dilute the precision of boundary features [39]. Therefore, inspired by the success of strip pooling, we employ it within our channel-gated module to specifically address this issue.

Specifically, we pass the input $\mathbf{I} \in \mathbb{R}^{D \times H \times W}$ through a series of simple convolutions, normalizations, and activation functions to obtain features $\mathbf{I}' \in \mathbb{R}^{D \times H \times W}$, which are then fed into the channel-gated module. The first step of the channel-gated module involves performing strip convolutions along the z , y , and x channels separately. The outputs $\mathbf{y}^d \in \mathbb{R}^D$, $\mathbf{y}^h \in \mathbb{R}^H$, and $\mathbf{y}^w \in \mathbb{R}^W$ for each corresponding channel can be

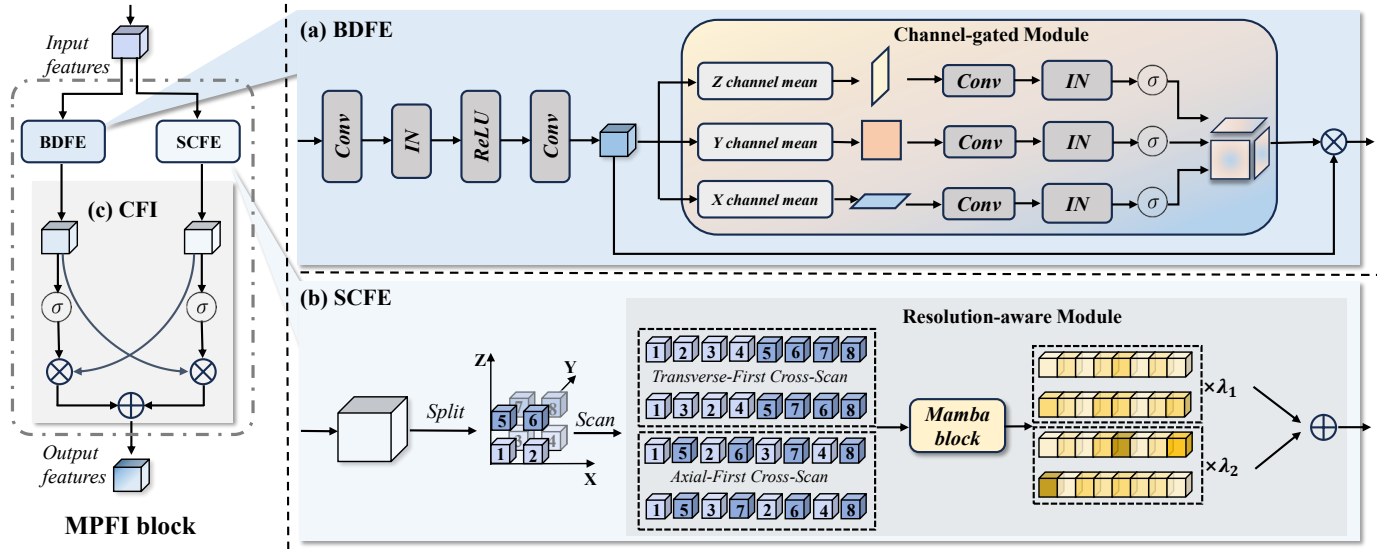


Fig. 3: Illustration of the Multi-Perspective Feature Interaction (MPFI) block. The MPFI block includes two feature extractors and a feature interaction module: (a) Boundary Discriminative Feature Extractor (BDFE), (b) Spatial Continuous Feature Extractor (SCFE), and (c) Cross Feature Interaction (CFI). Our MPFI block models neuronal affinity information from both local boundary discriminative features and global spatial continuity features.

represented as follows:

$$\mathbf{I}' = \text{Conv}(\text{ReLU}(\text{IN}(\text{Conv}(\mathbf{I})))) \quad (1)$$

$$\mathbf{y}_i^d = \frac{1}{H \times W} \sum_{0 \leq j < H, 0 \leq k < W} \mathbf{I}'_{i,j,k} \quad (2)$$

$$\mathbf{y}_j^h = \frac{1}{D \times W} \sum_{0 \leq i < D, 0 \leq k < W} \mathbf{I}'_{i,j,k} \quad (3)$$

$$\mathbf{y}_k^w = \frac{1}{D \times H} \sum_{0 \leq i < D, 0 \leq j < H} \mathbf{I}'_{i,j,k} \quad (4)$$

Unlike square pooling kernels, strip pooling in three dimensions generates long, narrow one-dimensional features that align with the elongated morphological characteristics of neuronal axons. These three features, \mathbf{y}^d , \mathbf{y}^h , and \mathbf{y}^w , encapsulate precise boundary information of neurons in three dimensions. Next, we apply 1D convolutions to interact with the three feature vectors, enhancing the representation of boundary information. The features are then normalized using an Instance Normalization (IN) layer and activated by a non-linear activation function to obtain boundary position features for each dimension.

$$\mathbf{z}^d = \sigma(\text{IN}(\text{Conv}^1(\mathbf{y}^d))) \quad (5)$$

$$\mathbf{z}^h = \sigma(\text{IN}(\text{Conv}^1(\mathbf{y}^h))) \quad (6)$$

$$\mathbf{z}^w = \sigma(\text{IN}(\text{Conv}^1(\mathbf{y}^w))) \quad (7)$$

In the description above, σ represents the sigmoid activation function, and Conv^1 denotes the one-dimensional convolution operation, where the parameters are shared across the three channels. The boundary position activation features \mathbf{z}^d , \mathbf{z}^h , and \mathbf{z}^w are multiplied by the original features \mathbf{I}' , using a gating mechanism to capture the regions of interest. Finally, we obtain the output of the BDFE, denoted as X_{local} , as shown

below:

$$X_{local} = \mathbf{I}' \times \mathbf{z}^d \times \mathbf{z}^h \times \mathbf{z}^w \quad (8)$$

C. SCFE: Spatial Continuous Feature Extractor

As established in previous sections, a core challenge in neuron segmentation is to model long-range spatial dependencies efficiently. While CNNs are limited by their local receptive fields, Transformer-based approaches, despite their global view, disrupt intrinsic spatial continuity by partitioning the data into patches. Furthermore, both architectures often exhibit inconsistent performance across EM datasets with varying degrees of anisotropy. This necessitates a novel architectural component capable of holistically capturing global voxel-level relationships without patching while dynamically adapting to varying data resolutions.

To this end, we base the SCFE on the Mamba architecture. The notable success of Mamba in its foundational domain—where, for instance, the Mamba-3B model has been shown to outperform Transformer-based models of equivalent size on language tasks [21]—motivates our investigation into its potential for neuronal reconstruction. A key advantage of Mamba is its linear complexity with respect to sequence length, which allows us to flatten an entire volumetric block into a single, long 1D sequence for processing. This obviates the need for patch partitioning—a strategy Transformers must employ to manage their quadratic complexity—thereby preserving intrinsic voxel-level spatial continuity.

However, while Mamba provides an ideal backbone, its standard scanning mechanisms are not inherently designed to handle the pronounced anisotropy of EM data. To address this limitation, we propose a novel resolution-aware module. This module employs a pair of specialized scanning mechanisms: a transverse-first cross-scan and an axial-first cross-scan, as illustrated in Fig. 3. This approach is explicitly designed

to differentiate between the high-resolution transverse planes (x-y) and the typically lower-resolution axial direction (z), allowing for a more nuanced modeling of anisotropic neuronal structures.

By design, this resolution-aware module dynamically adapts to varying data resolutions by leveraging the EM data's resolution as a prior. This prior enables the module to adjust the weights, λ_1 and λ_2 , for the transverse-first and axial-first scans, respectively. Consequently, with increasing anisotropy in the neuronal volume, the SCFE block assigns a greater weight to the axial-first cross-scan (λ_2) and a lesser weight to the transverse-first cross-scan (λ_1). This enhances the model's ability to capture the continuity of axial data. Therefore, we establish the following relationship between λ_1 and λ_2 :

$$\lambda_1 + \lambda_2 = 2 \quad (9)$$

$$\lambda_2 = \alpha D_{ani} + \beta \quad (10)$$

Here, α and β are hyperparameters. D_{ani} represents the degree of anisotropy in the EM data, which can be computed using the axial resolution R_a and transverse resolution R_t as follows:

$$D_{ani} = \frac{R_a}{R_t} \quad (11)$$

Specifically, we flatten the 3D input features using the transverse-first cross-directional scanning mechanism to obtain \mathbf{z}_1^t and \mathbf{z}_2^t , and the axial-first cross-directional scanning mechanism to obtain \mathbf{z}_1^a and \mathbf{z}_2^a , where t denotes transverse and a denotes axial. These four sequences are then processed by the Mamba layer (denoted as M) to model global information. Subsequently, feature interactions are performed to obtain the SCFE output, denoted as X_{global} .

$$X_{global} = \lambda_1 M(\mathbf{z}_1^t) + \lambda_1 M(\mathbf{z}_2^t) + \lambda_2 M(\mathbf{z}_1^a) + \lambda_2 M(\mathbf{z}_2^a) \quad (12)$$

D. CFI: Cross Feature Interaction

EM volumes typically contain neuron instances that span a wide range of scales, from large, continuous structures to small, intricate fragments. The local boundary features from the BDFE are essential for delineating these smaller instances, while the global continuity features from the SCFE are crucial for maintaining the integrity of larger ones. To address the challenge of effectively integrating these two perspectives, we introduce a dynamic feature interaction mechanism. In contrast to direct, addition-based fusion methods, our approach employs cross-modulation, which enables the model to adaptively process neurons of varying scales by dynamically modulating the interplay between local and global feature maps.

This interaction can be conceptualized as a reciprocal enhancement process, as illustrated in Fig. 3(c). The global continuity map (X_{global}) serves as a spatial attention mechanism for the local boundary features (X_{local}), thereby enhancing feature salience in regions corresponding to large, continuous structures. Conversely, the local boundary map provides high-frequency details to refine the global features, thereby improving the precision of affinity predictions in structurally complex regions.

Specifically, given the local features X_{local} from Eq. (8) and the global features X_{global} from Eq. (12), a reciprocal

modulation is performed. This modulation is implemented by using each feature map to gate the other via a sigmoid function (σ), where \odot denotes the element-wise Hadamard product:

$$X'_{local} = X_{local} \odot \sigma(X_{global}) = X_{local} \odot \frac{1}{1 + e^{-X_{global}}} \quad (13)$$

$$X'_{global} = X_{global} \odot \sigma(X_{local}) = X_{global} \odot \frac{1}{1 + e^{-X_{local}}} \quad (14)$$

Following cross-modulation, the resulting representations X'_{local} and X'_{global} each integrate information from the complementary perspective. These modulated representations are then summed to produce the final output of the MPFI block, O_{MPFI} , which is synergistically enriched from both perspectives:

$$O_{MPFI} = X'_{local} + X'_{global} \quad (15)$$

This synergy enriches the final feature representation from both local and global perspectives, yielding more robust and accurate affinity predictions across multiple scales.

IV. EXPERIMENTS

A. Datasets

AC3/AC4. This dataset [40] consists of two volumes cropped from the mouse somatosensory cortex imaged using scanning electron microscopy (SEM). The sizes of the AC3 and AC4 volumes are $256 \times 1024 \times 1024$ and $100 \times 1024 \times 1024$, respectively, with a resolution of $6 \times 6 \times 29 \text{ nm}^3$. We use the top 80 slices of AC4 for training and the top 100 slices of AC3 for testing.

CREMI. The CREMI dataset [41] originates from the brain of an adult Drosophila fly, imaged using serial section transmission EM (ssTEM) at a resolution of $4 \times 4 \times 40 \text{ nm}^3$. The dataset includes three labeled subsets (CREMI-A/B/C), each consisting of 125 consecutive slices. We use the top 60 slices of each subset for training and the bottom 50 slices for testing.

FIB25. Unlike the previous two anisotropic datasets, the FIB25 dataset [42] images the Drosophila brain using focused ion beam SEM (FIB-SEM) at an isotropic resolution of 8 nm. Two volumes, each of size $520 \times 520 \times 520$, are used for training and testing, respectively.

Kasthuri. The Kasthuri dataset [40] has a size of $1850 \times 10747 \times 12895$ with a voxel resolution of $6 \times 6 \times 29 \text{ nm}^3$. In this work, we cropped a subset of size $300 \times 4096 \times 4096$ from the Kasthuri dataset, guided by the spatial distribution of annotated neurons. The bounding box of this subset spans from (1050, 6500, 3200) to (1350, 10596, 7296). We used AC4 for training and evaluated large-volume neuron segmentation on this subset.

B. Metrics

We use two widely adopted metrics to evaluate neuron segmentation performance in EM images: variation of information (VI) and adapted Rand error (ARAND). Lower values of these metrics indicate better segmentation quality.

Methods	Waterz [11]				Multicut [15]			
	VI _s ↓	VI _m ↓	VI ↓	ARAND ↓	VI _s ↓	VI _m ↓	VI ↓	ARAND ↓
AC3/AC4	MALA [11]	0.892	0.331	1.224	0.135	0.827	0.406	1.233
	Superhuman [10]	0.770	0.289	<u>1.059</u>	<u>0.108</u>	0.794	0.316	1.110
	PEA [27]	0.812	0.285	1.097	0.118	0.728	0.396	1.124
	LSD [25]	0.923	0.320	1.246	0.122	0.982	0.348	1.330
	UNETR [19]	0.952	0.812	1.765	0.334	0.931	0.992	1.922
	SwinUNETR [20]	0.873	0.490	1.364	0.238	0.841	0.425	1.266
	U-Mamba [32]	0.875	0.297	1.171	0.124	0.800	0.313	1.114
	SegMamba [33]	0.801	0.287	1.088	0.109	0.796	0.286	<u>1.082</u>
	EMMamba [35]	0.906	0.411	1.317	0.138	0.815	0.595	1.411
CREMI-A	Ours	0.752	0.269	1.020	0.104	0.712	0.259	0.971
	MALA [11]	0.509	0.475	0.984	0.204	0.505	0.437	0.942
	Superhuman [10]	0.515	0.463	0.978	0.190	0.517	0.432	0.949
	PEA [27]	0.530	0.390	<u>0.920</u>	0.186	<u>0.557</u>	0.378	<u>0.935</u>
	LSD [25]	0.489	0.440	<u>0.929</u>	<u>0.183</u>	0.569	0.466	1.035
	UNETR [19]	0.777	1.027	1.805	0.444	0.558	0.728	1.286
	SwinUNETR [20]	0.721	0.819	1.540	0.365	0.540	0.525	1.066
	U-Mamba [32]	0.565	0.509	1.074	0.224	0.521	0.482	1.003
	SegMamba [33]	0.565	0.566	1.131	0.247	0.513	0.494	1.007
CREMI-B	EMMamba [35]	0.610	0.693	1.303	0.287	0.529	0.594	1.122
	Ours	0.477	0.388	0.865	0.142	0.484	0.370	0.853
	MALA [11]	0.931	0.655	1.586	0.170	1.039	0.351	1.391
	Superhuman [10]	0.696	0.873	<u>1.569</u>	0.185	0.930	0.432	<u>1.362</u>
	PEA [27]	0.942	0.326	1.268	0.080	1.213	0.232	1.446
	LSD [25]	1.561	0.789	2.350	0.285	1.848	0.770	2.618
	UNETR [19]	2.337	3.091	5.428	0.763	2.303	0.821	3.124
	SwinUNETR [20]	1.754	1.488	3.243	0.418	2.187	0.551	2.738
	U-Mamba [32]	0.984	0.825	1.809	0.223	1.080	0.599	1.679
CREMI-C	SegMamba [33]	1.036	1.202	2.239	0.322	1.126	0.612	1.738
	EMMamba [35]	1.389	1.667	3.056	0.458	1.177	1.093	2.270
	Ours	0.713	0.556	1.268	0.087	0.898	0.408	1.305
	MALA [11]	1.026	0.635	1.661	0.195	0.967	0.560	1.527
	Superhuman [10]	0.998	0.475	<u>1.473</u>	0.142	0.951	0.516	1.467
	PEA [27]	1.299	0.252	<u>1.551</u>	<u>0.135</u>	1.066	0.360	1.426
	LSD [25]	1.095	0.583	1.678	0.190	1.189	0.694	1.883
	UNETR [19]	1.388	1.412	2.800	0.358	1.238	0.774	2.012
	SwinUNETR [20]	1.267	1.021	2.288	0.297	1.262	0.748	2.010

TABLE I: Quantitative comparisons of different methods on the AC3/AC4 and CREMI datasets. Green, orange and blue backgrounds indicate CNN-based, Transformer-based, and Mamba-based methods, respectively. **Bold** and underlined items indicate the first and second scoring results.

C. Implementation Details

Each model is trained on a single NVIDIA V100 GPU with the Adam optimizer. All models are trained for 200,000 epochs with a fixed learning rate of 0.0001 and a batch size of 2.

D. Comparison with State-of-the-art Methods

We compared several state-of-the-art methods, including CNN-based methods (MALA, Superhuman, PEA, and LSD), Transformer-based methods (UNETR and SwinUNETR), and Mamba-based methods (U-Mamba, SegMamba, and EMMamba). All methods were trained and evaluated using block shapes consistent with those reported in the original papers, with slight adjustments along the z -axis to accommodate the limited number of slices in the EM datasets. Specifically,

MALA uses [53, 268, 268], Superhuman, PEA, and LSD use [18, 160, 160], UNETR and SwinUNETR use [64, 96, 96], and U-Mamba, SegMamba, and EMMamba use [32, 128, 128]. The block shape used in our method is [18, 160, 160]. During inference, we adopt a tiling strategy with overlapping blocks, where the overlap along each dimension is set to half of its corresponding block size. After predicting the affinity map, two standard post-processing techniques were applied: Waterz [11] and Multicut [15].

Quantitative Analysis. The quantitative results, presented across Tables I, II, and III, demonstrate that NeuroMamba consistently achieves state-of-the-art performance across all evaluated benchmarks. As highlighted in Tab. I, on the particularly challenging CREMI-A benchmark, NeuroMamba yields

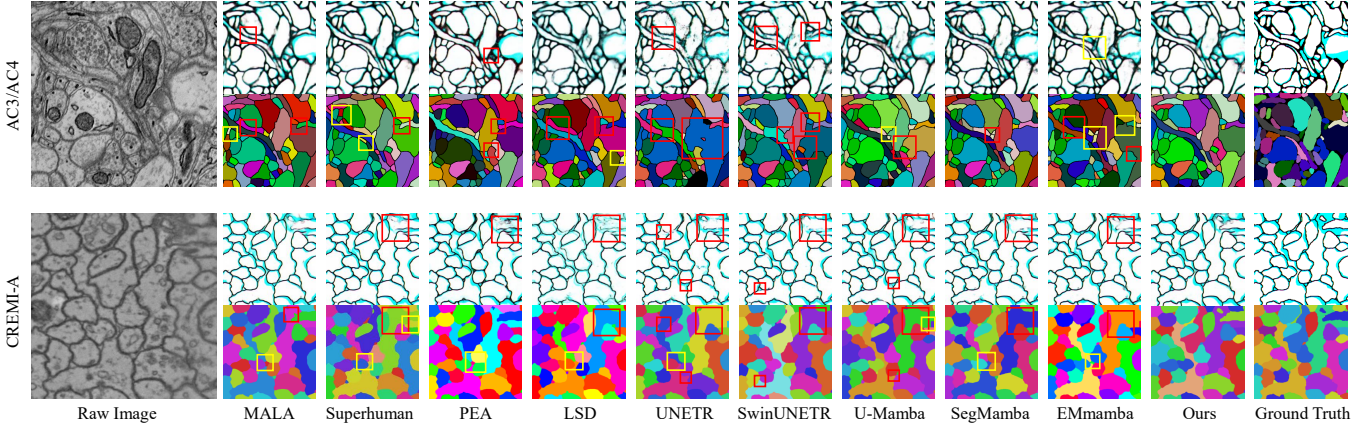


Fig. 4: 2D visualization results on AC3/AC4 and CREMI-A data. The left side shows the EM raw image, and the right side shows the affinity and segmentation results. The red and yellow boxes indicate merge and split errors, respectively

Methods	Multicut [15]				
	VI _s ↓	VI _m ↓	VI ↓	ARAND ↓	
MALA [11]	1.098	1.056	2.154	0.216	
FIB25	Superhuman [10]	1.071	0.888	1.959	0.166
	PEA [27]	0.950	1.017	1.967	0.200
	LSD [25]	1.217	0.821	2.038	0.181
	UNETR [19]	1.008	0.915	1.923	<u>0.162</u>
	SwinUNETR [20]	1.014	0.901	<u>1.915</u>	0.168
	U-Mamba [32]	1.058	0.897	1.955	0.173
	SegMamba [33]	1.060	0.866	1.926	0.167
	EMmamba [35]	1.068	0.926	1.994	0.177
	Ours	1.041	0.851	1.893	0.159

TABLE II: Quantitative comparisons of different methods on the FIB25 datasets. **Bold** and underlined items indicate the first and second scoring results.

Methods	Waterz		Multicut		
	VI ↓	ARAND ↓	VI ↓	ARAND ↓	
Kasthuri	Superhuman [10]	0.840	0.320	<u>0.829</u>	<u>0.325</u>
	PEA [27]	0.843	0.324	<u>1.098</u>	0.350
	LSD [25]	0.860	0.298	1.213	0.489
	SwinUNETR [20]	1.259	0.605	1.148	0.538
	SegMamba [33]	0.910	0.436	0.974	0.512
	Ours	0.787	<u>0.303</u>	0.761	0.301

TABLE III: Quantitative comparisons of different methods on the Kasthuri datasets. **Bold** and underlined items indicate the first and second scoring results.

substantial relative ARAND improvements of **22.4%** and **21.7%** with Waterz and Multicut post-processing, respectively. This robustness and generalization are further substantiated in Tab. II, where our approach secures state-of-the-art results on both isotropic (FIB25) and anisotropic datasets, underscoring its adaptability to varying data resolutions. The superior performance on the large-scale Kasthuri dataset (Tab. III) further affirms the scalability and suitability of our method for large-volume, real-world reconstruction tasks.

Qualitative Analysis. The visual comparisons in Figs. 4 and 6 provide qualitative evidence of our method’s superior per-

Methods	Params(M)	FLOPs(G)	Latency(s)	ARAND ↓
MALA [11]	84.0	413.6	0.027	0.179
Superhuman [10]	1.6	185.9	0.046	0.176
PEA [27]	2.1	177.2	0.044	<u>0.175</u>
LSD [25]	1.6	186.1	0.046	0.217
UNETR [19]	115.2	752.3	0.060	0.314
SwinUNETR [20]	62.0	440.3	0.068	0.224
U-Mamba [32]	3.51	620.1	0.063	0.201
SegMamba [33]	64.2	1213.9	0.067	0.201
EMmamba [35]	26.8	323.3	0.054	0.277
Ours	2.1	220.8	0.059	0.137

TABLE IV: Efficiency comparison of different methods on CREMI-A.

formance. In both 2D and 3D visualizations, reconstructions generated by NeuroMamba exhibit significantly improved overall continuity and accurately segment fine structures that prove challenging for competing methods. This significant improvement is directly attributable to the synergy between our core components: the BDFF module, which enhances feature representation in ambiguous boundary regions, and the SCFE module, which incorporates global contextual information for each neuron. This effective fusion of fine-grained boundary cues with global spatial connectivity is pivotal in achieving more complete and accurate neuron reconstructions.

Model Complexity Comparison. As shown in Tab. IV, we compare the model complexity of various state-of-the-art methods. The inference latency is measured as the time required to process a standardized volume of size [64, 96, 96]. Our model achieves superior performance while maintaining a parameter count and computational cost comparable to lightweight CNNs. Compared with other Transformer-based and Mamba-based methods, NeuroMamba requires fewer parameters and floating-point operations. The inference latency of NeuroMamba is higher than that of CNN-based methods but lower than that of most Transformer-based and Mamba-based methods.

BDFE	SCFE	Waterz		Multicut	
		VI \downarrow	ARAND \downarrow	VI \downarrow	ARAND \downarrow
✓	✓	0.895	0.163	0.906	0.169
		0.889	0.158	0.867	0.145
		0.892	0.158	0.886	0.152
✓	✓	0.865	0.142	0.853	0.137

(a) Ablation of BDFE and SCFE.

Datasets	VI \downarrow		ARAND \downarrow	
	w/o Pri.	w Pri.	w/o Pri.	w Pri.
AC3/AC4	1.002	0.971	0.101	0.090
CREMI-A	0.859	0.853	0.140	0.137
FIB25	1.926	1.893	0.161	0.159

(c) Ablation of resolution-aware module.

Methods	VI \downarrow		ARAND \downarrow	
	VI \downarrow	ARAND \downarrow	VI \downarrow	ARAND \downarrow
UNETR	1.286	0.314		
UNEM	1.278	0.281		
Ours	0.853	0.137		

(d) Effectiveness of Mamba.

Methods	Waterz		Multicut	
	VI \downarrow	ARAND \downarrow	VI \downarrow	ARAND \downarrow
addition	0.915	0.168	0.852	0.142
multiplication	0.929	0.169	0.894	0.154
concatenation	0.889	0.158	0.869	0.150
interaction	0.865	0.142	0.853	0.137

(b) Ablation of CFI.

Methods	VI \downarrow		ARAND \downarrow	
	VI \downarrow	ARAND \downarrow	VI \downarrow	ARAND \downarrow
Square Pooling	0.860	0.146		
Strip Pooling	0.853	0.137		

(e) Ablation of strip pooling.

TABLE V: Ablation studies and comparison analysis.

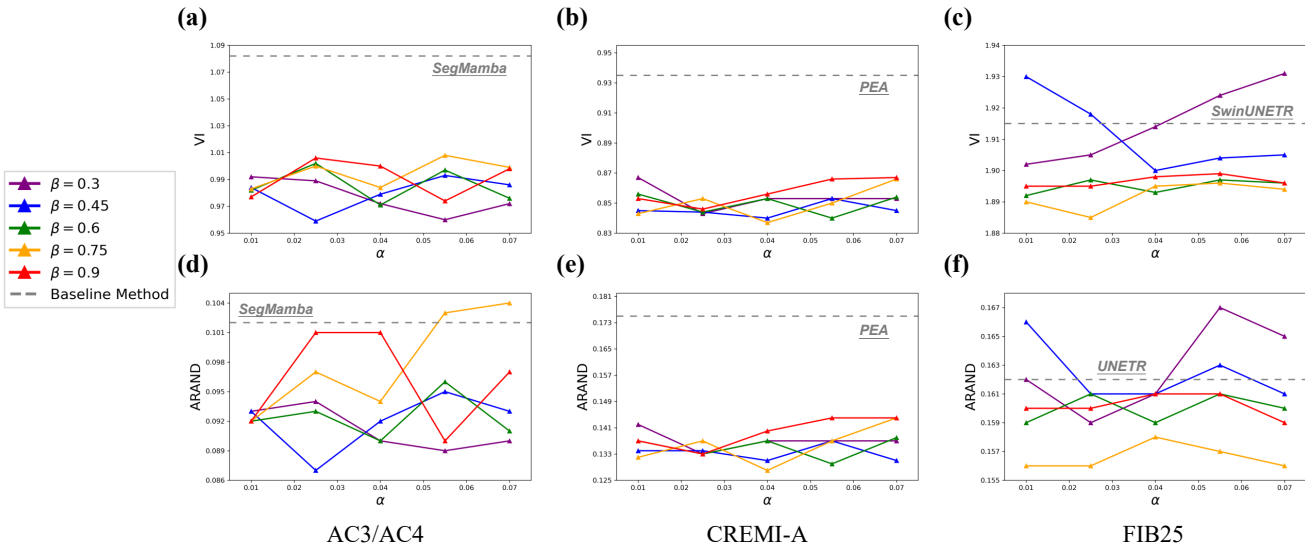


Fig. 5: We evaluate the performance of our model under different hyperparameter configurations on three datasets. The top row reports the VI metric, while the bottom row presents the ARAND metric. The best-performing baseline method and its performance are highlighted in the figure.

E. Ablation Studies and Analysis

To validate the effectiveness of our method, we conducted a series of ablation studies on different datasets.

Effectiveness of Main Components. We first validated the effectiveness of the BDFE and SCFE modules. Tab. Va presents the experimental results under different module configurations, demonstrating that an optimal neuron segmentation model requires the joint modeling of both global spatial continuous and local boundary discriminative information. Next, we examined the efficacy of the CFI module’s information interaction. Specifically, we compared it against three commonly used information fusion methods: addition, element-wise multiplication, and concatenation. The results in Tab. Vb indicate that the information interaction method based on cross-modulation can dynamically adjust the weights of global spatial continuous and local boundary discriminative features,

enabling the model to more flexibly handle neuron instances of varying scales.

Effectiveness of Resolution-aware Modules. To validate that introducing resolution prior information enables the model to better adapt to data with different resolutions, we conducted ablation experiments on multiple datasets. As shown in Tab. Vc, our model achieves improved performance across different datasets after incorporating resolution prior information.

Effectiveness of Mamba. Transformer-based methods require partitioning 3D blocks into patches, which neglects the spatial relationships between voxels within each block and leads to the loss of affinity information. Our proposed NeuroMamba models the relationships among all voxels without patch partitioning, effectively mitigating this issue. As shown in Tab. Vd, we first replace the transformer block in UNETR with the Mamba block to obtain UNEM. The comparative exper-

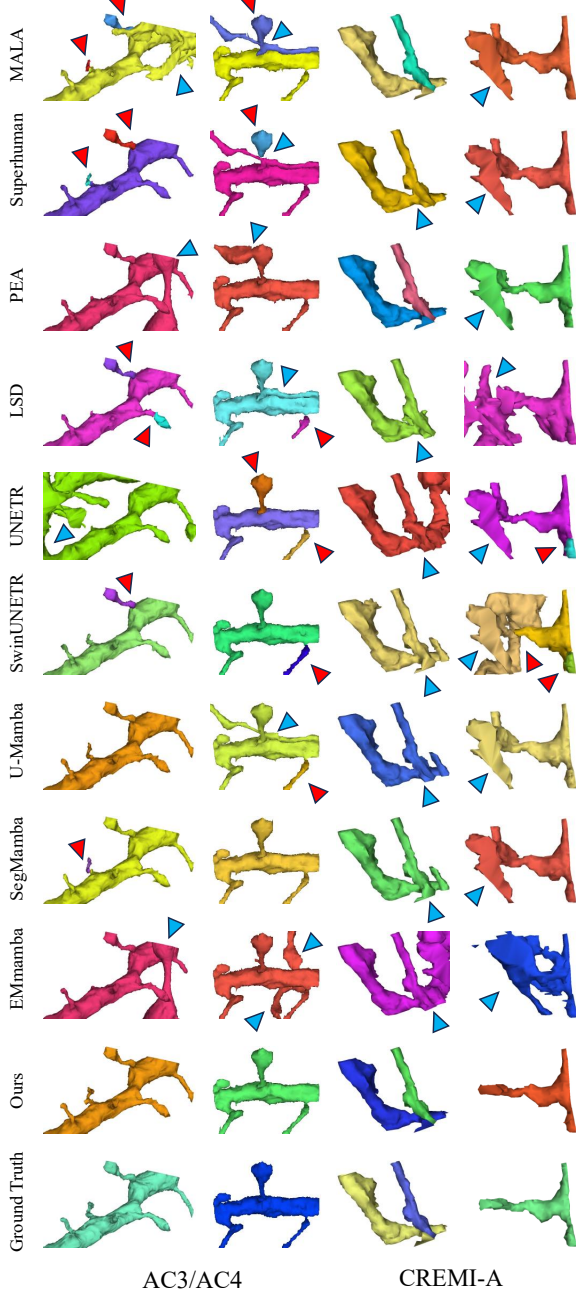


Fig. 6: 3D visualization results on AC3/AC4 and CREMI-A data. The blue and red arrows indicate merge and split errors, respectively.

iments demonstrate that the Mamba block can better capture long-range neuronal dependencies. However, its performance remains significantly inferior to that of NeuroMamba, which simultaneously models both global voxel-level information and local spatial proximity.

Effectiveness of Strip Pooling. As shown in Tab. Ve, replacing strip pooling with square pooling in NeuroMamba leads to a decrease in performance. This finding indicates that strip pooling is better suited to the elongated morphological characteristics of neurons.

Robustness Across Different Block Shapes. As shown in

block shape	Best baseline (VI/ARAND)	Ours (VI/ARAND)
[18,160,160]	0.935 / 0.175	0.853 / 0.137
[64,96,96]	1.066 / 0.224	0.845 / 0.134
[32,128,128]	1.003 / 0.201	0.851 / 0.133

TABLE VI: Results under different block shapes.

Methods	Waterz		Multicut	
	VI ↓	ARAND ↓	VI ↓	ARAND ↓
<i>Uni</i> [*]	0.899	0.170	0.878	0.151
<i>Uni</i> [†]	0.903	0.161	0.858	0.144
<i>Uni</i> [*] + <i>Uni</i> [†]	0.899	0.167	0.862	0.141
<i>Bi</i> [*]	0.907	0.172	0.890	0.157
<i>Bi</i> [†]	0.906	0.168	0.883	0.150
<i>Bi</i> [*] + <i>Bi</i> [†]	0.910	0.159	0.876	0.147
<i>Cro</i> [*]	0.884	0.169	0.855	0.139
<i>Cro</i> [†]	0.885	0.155	0.868	0.143
<i>Cro</i> [*] + <i>Cro</i> [†]	0.865	0.142	0.853	0.137
Dual-scale	0.891	0.166	0.856	0.140
Multi-scale	0.924	0.168	0.882	0.152
Hilbert	0.872	0.146	0.883	0.151

TABLE VII: Ablation of different scanning mechanisms on CREMI-A. 'Uni' represents Unidirectional Scan, 'Bi' represents Bidirectional Scan, and 'Cro' represents Cross-Scan. '*' indicates Transverse-First, while '†' indicates Axial-First.

Tab. VI, NeuroMamba achieves comparable performance on CREMI-A across different block shapes. In each block-shape configuration, NeuroMamba consistently outperforms its corresponding baseline.

Different Scanning Mechanisms. To demonstrate the suitability of our proposed cross-scan mechanisms for modeling transverse and axial features in 3D EM data, we conducted comparative experiments with unidirectional and bidirectional scanning strategies [28], [36]. We further compared methods employing Dual-scale [37] and Multi-scale [43] scanning strategies, as well as the Hilbert scanning technique [37], [38], which has demonstrated strong performance in detection tasks. As shown in Tab. VII, our proposed transverse-first and axial-first cross-scan mechanisms achieve the best performance. This may be attributed to the fact that the cross-scan strategy effectively mitigates the asymmetry introduced by one-dimensional unwrapping, while scanning in both transverse and axial directions allows the model to better capture structural information along multiple orientations.

Ablation Experiments on Hyperparameter Tuning. The SCFE module dynamically adjusts the weights λ_1 and λ_2 based on the resolution prior of the EM data, as shown in 9 and 10. As shown in Fig.5, we conducted experiments under multiple parameter settings across the three datasets. The parameter α is set to $\{0.01, 0.025, 0.04, 0.055, 0.07\}$, and β is set to $\{0.3, 0.45, 0.6, 0.75, 0.9\}$. Our model consistently outperforms the best-performing baseline in most parameter configurations, demonstrating its robustness to hyperparameter variation. Finally, we adopt $\alpha = 0.04$ and $\beta = 0.6$ as they yield the most stable performance across the three datasets.

V. CONCLUSION

In this paper, we have presented NeuroMamba, a novel multi-perspective framework for neuron segmentation in volumetric EM data. By identifying the complementary weaknesses of existing methods, we developed a synergistic architecture that integrates a channel-gated module (BDFE) for boundary discriminative features and a resolution-aware Mamba-based module (SCFE) to efficiently model long-range spatial continuity without patching. These multi-perspective features are dynamically fused via a cross-modulation mechanism. Extensive experiments on four public benchmarks demonstrate the superiority and robustness of our method, culminating in a relative improvement of 22.4% in the ARAND metric on the challenging CREMI-A dataset, establishing a new state-of-the-art performance.

REFERENCES

- [1] J. Ngai, “Brain 2.0: Transforming neuroscience,” *Cell*, vol. 185, no. 1, pp. 4–8, 2022.
- [2] D. G. C. Hildebrand, M. Cicconet, R. M. Torres, W. Choi, T. M. Quan, J. Moon, A. W. Wetzel, A. Scott Champion, B. J. Graham, O. Randlett *et al.*, “Whole-brain serial-section electron microscopy in larval zebrafish,” *Nature*, vol. 545, no. 7654, pp. 345–349, 2017.
- [3] A. Motta, M. Berning, K. M. Boergens, B. Staffler, M. Beining, S. Loomba, P. Hennig, H. Wissler, and M. Helmstaedter, “Dense connectomic reconstruction in layer 4 of the somatosensory cortex,” *Science*, vol. 366, no. 6469, p. eaay3134, 2019.
- [4] N. L. Turner, T. Macrina, J. A. Bae, R. Yang, A. M. Wilson, C. Schneider-Mizell, K. Lee, R. Lu, J. Wu, A. L. Bodor *et al.*, “Reconstruction of neocortex: Organelles, compartments, cells, circuits, and activity,” *Cell*, vol. 185, no. 6, pp. 1082–1100, 2022.
- [5] C. J. Peddie and L. M. Collinson, “Exploring the third dimension: volume electron microscopy comes of age,” *Micron*, vol. 61, pp. 9–19, 2014.
- [6] C. J. Peddie, C. Genoud, A. Kreshuk, K. Meechan, K. D. Micheva, K. Narayan, C. Pape, R. G. Parton, N. L. Schieber, Y. Schwab *et al.*, “Volume electron microscopy,” *Nature Reviews Methods Primers*, vol. 2, no. 1, p. 51, 2022.
- [7] L. F. Abbott, D. D. Bock, E. M. Callaway, W. Denk, C. Dulac, A. L. Fairhall, I. Fiete, K. M. Harris, M. Helmstaedter, V. Jain *et al.*, “The mind of a mouse,” *Cell*, vol. 182, no. 6, pp. 1372–1376, 2020.
- [8] A. Shapson-Coe, M. Januszewski, D. R. Berger, A. Pope, Y. Wu, T. Blakely, R. L. Schalek, P. H. Li, S. Wang, J. Maitlin-Shepard *et al.*, “A petavoxel fragment of human cerebral cortex reconstructed at nanoscale resolution,” *Science*, vol. 384, no. 6696, p. eadk4858, 2024.
- [9] L. K. Scheffer, C. S. Xu, M. Januszewski, Z. Lu, S.-y. Takemura, K. J. Hayworth, G. B. Huang, K. Shinomiya, J. Maitlin-Shepard, S. Berg *et al.*, “A connectome and analysis of the adult drosophila central brain,” *elife*, vol. 9, p. e57443, 2020.
- [10] K. Lee, J. Zung, P. Li, V. Jain, and H. S. Seung, “Superhuman accuracy on the snemi3d connectomics challenge,” *arXiv preprint arXiv:1706.00120*, 2017.
- [11] J. Funke, F. Tschopp, W. Grisaitis, A. Sheridan, C. Singh, S. Saalfeld, and S. C. Turaga, “Large scale image segmentation with structured loss based deep learning for connectome reconstruction,” *IEEE transactions on pattern analysis and machine intelligence*, vol. 41, no. 7, pp. 1669–1680, 2018.
- [12] M. Januszewski, J. Kornfeld, P. H. Li, A. Pope, T. Blakely, L. Lindsey, J. Maitlin-Shepard, M. Tyka, W. Denk, and V. Jain, “High-precision automated reconstruction of neurons with flood-filling networks,” *Nature methods*, vol. 15, no. 8, pp. 605–610, 2018.
- [13] K. Lee, R. Lu, K. Luther, and H. S. Seung, “Learning and segmenting dense voxel embeddings for 3d neuron reconstruction,” *IEEE transactions on medical imaging*, vol. 40, no. 12, pp. 3801–3811, 2021.
- [14] S. C. Turaga, J. F. Murray, V. Jain, F. Roth, M. Helmstaedter, K. Briggman, W. Denk, and H. S. Seung, “Convolutional networks can learn to generate affinity graphs for image segmentation,” *Neural computation*, vol. 22, no. 2, pp. 511–538, 2010.
- [15] T. Beier, C. Pape, N. Rahaman, T. Prange, S. Berg, D. D. Bock, A. Cardona, G. W. Knott, S. M. Plaza, L. K. Scheffer *et al.*, “Multicut brings automated neurite segmentation closer to human performance,” *Nature methods*, vol. 14, no. 2, pp. 101–102, 2017.
- [16] Z. Li, X. Yang, J. Liu, B. Hong, Y. Zhang, H. Zhai, L. Shen, X. Chen, Z. Liu, and H. Han, “Deepmulticut: Deep learning of multicut problem for neuron segmentation from electron microscopy volume,” *IEEE Transactions on Pattern Analysis and Machine Intelligence*, 2024.
- [17] Y. Chen, W. Huang, S. Zhou, Q. Chen, and Z. Xiong, “Self-supervised neuron segmentation with multi-agent reinforcement learning,” in *Proceedings of the Thirty-Second International Joint Conference on Artificial Intelligence*, 2023, pp. 609–617.
- [18] R. Sun, N. Luo, Y. Pan, H. Mai, T. Zhang, Z. Xiong, and F. Wu, “Appearance prompt vision transformer for connectome reconstruction,” in *Proceedings of the Thirty-Second International Joint Conference on Artificial Intelligence*, 2023, pp. 1423–1431.
- [19] A. Hatamizadeh, Y. Tang, V. Nath, D. Yang, A. Myronenko, B. Landman, H. R. Roth, and D. Xu, “Unetr: Transformers for 3d medical image segmentation,” in *Proceedings of the IEEE/CVF winter conference on applications of computer vision*, 2022, pp. 574–584.
- [20] A. Hatamizadeh, V. Nath, Y. Tang, D. Yang, H. R. Roth, and D. Xu, “Swin unetr: Swin transformers for semantic segmentation of brain tumors in mri images,” in *International MICCAI brainlesion workshop*. Springer, 2021, pp. 272–284.
- [21] A. Gu and T. Dao, “Mamba: Linear-time sequence modeling with selective state spaces,” *arXiv preprint arXiv:2312.00752*, 2023.
- [22] R. E. Kalman, “A new approach to linear filtering and prediction problems,” 1960.
- [23] Y. Meirovitch, L. Mi, H. Saribekyan, A. Matveev, D. Rolnick, and N. Shavit, “Cross-classification clustering: An efficient multi-object tracking technique for 3-d instance segmentation in connectomics,” in *Proceedings of the IEEE/CVF Conference on Computer Vision and Pattern Recognition*, 2019, pp. 8425–8435.
- [24] M. Schmidt, A. Motta, M. Sievers, and M. Helmstaedter, “Roboem: automated 3d flight tracing for synaptic-resolution connectomics,” *Nature Methods*, vol. 21, no. 5, pp. 908–913, 2024.
- [25] A. Sheridan, T. M. Nguyen, D. Deb, W.-C. A. Lee, S. Saalfeld, S. C. Turaga, U. Manor, and J. Funke, “Local shape descriptors for neuron segmentation,” *Nature methods*, vol. 20, no. 2, pp. 295–303, 2023.
- [26] C. Xiao, B. Hong, J. Liu, Y. Tang, Q. Xie, and H. Han, “Deep residual contextual and subpixel convolution network for automated neuronal structure segmentation in micro-connectomics,” *Computer Methods and Programs in Biomedicine*, vol. 219, p. 106759, 2022.
- [27] W. Huang, S. Deng, C. Chen, X. Fu, and Z. Xiong, “Learning to model pixel-embedded affinity for homogeneous instance segmentation,” in *Proceedings of the AAAI Conference on Artificial Intelligence*, vol. 36, no. 1, 2022, pp. 1007–1015.
- [28] L. Zhu, B. Liao, Q. Zhang, X. Wang, W. Liu, and X. Wang, “Vision mamba: Efficient visual representation learning with bidirectional state space model,” *arXiv preprint arXiv:2401.09417*, 2024.
- [29] T. Huang, X. Pei, S. You, F. Wang, C. Qian, and C. Xu, “Localmamba: Visual state space model with windowed selective scan,” *arXiv preprint arXiv:2403.09338*, 2024.
- [30] X. Pei, T. Huang, and C. Xu, “Efficientmamba: Atrous selective scan for light weight visual mamba,” *arXiv preprint arXiv:2403.09977*, 2024.
- [31] C. Yang, Z. Chen, M. Espinosa, L. Ericsson, Z. Wang, J. Liu, and E. J. Crowley, “Plainmamba: Improving non-hierarchical mamba in visual recognition,” *arXiv preprint arXiv:2403.17695*, 2024.
- [32] J. Ma, F. Li, and B. Wang, “U-mamba: Enhancing long-range dependency for biomedical image segmentation,” *arXiv preprint arXiv:2401.04722*, 2024.
- [33] Z. Xing, T. Ye, Y. Yang, G. Liu, and L. Zhu, “Segmamba: Long-range sequential modeling mamba for 3d medical image segmentation,” *arXiv preprint arXiv:2401.13560*, 2024.
- [34] A. Archit and C. Pape, “Vim-unet: Vision mamba for biomedical segmentation,” *arXiv preprint arXiv:2404.07705*, 2024.
- [35] Y. Chen, H. Shi, X. Liu, T. Shi, R. Zhang, D. Liu, Z. Xiong, and F. Wu, “Tokenunify: Scalable autoregressive visual pre-training with mixture token prediction,” *arXiv preprint arXiv:2405.16847*, 2024.
- [36] K. Li, X. Li, Y. Wang, Y. He, Y. Wang, L. Wang, and Y. Qiao, “Videomamba: State space model for efficient video understanding,” *arXiv preprint arXiv:2403.06977*, 2024.
- [37] G. Zhang, L. Fan, C. He, Z. Lei, Z. Zhang, and L. Zhang, “Voxel mamba: Group-free state space models for point cloud based 3d object detection,” *arXiv preprint arXiv:2406.10700*, 2024.

- [38] H. He, Y. Bai, J. Zhang, Q. He, H. Chen, Z. Gan, C. Wang, X. Li, G. Tian, and L. Xie, "Mambaad: Exploring state space models for multi-class unsupervised anomaly detection," *arXiv preprint arXiv:2404.06564*, 2024.
- [39] Q. Hou, L. Zhang, M.-M. Cheng, and J. Feng, "Strip pooling: Rethinking spatial pooling for scene parsing," in *Proceedings of the IEEE/CVF conference on computer vision and pattern recognition*, 2020, pp. 4003–4012.
- [40] N. Kasthuri, K. J. Hayworth, D. R. Berger, R. L. Schalek, J. A. Conchello, S. Knowles-Barley, D. Lee, A. Vázquez-Reina, V. Kaynig, T. R. Jones *et al.*, "Saturated reconstruction of a volume of neocortex," *Cell*, vol. 162, no. 3, pp. 648–661, 2015.
- [41] Z. Zheng, J. S. Lauritzen, E. Perlman, C. G. Robinson, M. Nichols, D. Milkie, O. Torrens, J. Price, C. B. Fisher, N. Sharifi *et al.*, "A complete electron microscopy volume of the brain of adult *drosophila melanogaster*," *Cell*, vol. 174, no. 3, pp. 730–743, 2018.
- [42] S.-y. Takemura, C. S. Xu, Z. Lu, P. K. Rivlin, T. Parag, D. J. Olbris, S. Plaza, T. Zhao, W. T. Katz, L. Umayam *et al.*, "Synaptic circuits and their variations within different columns in the visual system of *drosophila*," *Proceedings of the National Academy of Sciences*, vol. 112, no. 44, pp. 13 711–13 716, 2015.
- [43] Y. Shi, M. Dong, and C. Xu, "Multi-scale vmamba: Hierarchy in hierarchy visual state space model," *arXiv preprint arXiv:2405.14174*, 2024.